Diffusion-Weighted and Dynamic Contrast-Enhanced MRI Derived Imaging Metrics for Stereotactic Body Radiotherapy of Pancreatic Ductal Adenocarcinoma: Preliminary Findings

Richard Kinh Do[1], Marsha Reyngold[2], Ramesh Paudyal[3], Jung Hun Oh[3], Amaresha Shridhar Konar[3], Eve LoCastro[3], Karyn A. Goodman[4], and Amita Shukla-Dave[1,3]

Departments of [1]Radiology; [2]Radiation Oncology; [3]Medical Physics, Memorial Sloan Kettering Cancer Center, New York, NY; and [4]Tisch Cancer Institute at Mount Sinai Hospital, New York, NY

Corresponding Author:
Amita Shukla-Dave, PhD, FISMRM
Departments of Medical Physics and Radiology, Memorial Sloan Kettering Cancer Center, 1275 York Avenue, New York, New York 10065;
E-mail: davea@mskcc.org

Key Words: Quantitative imaging, diffusion-weighted, dynamic contrast-enhanced, shutter-speed model, pancreatic ductal adenocarcinoma, stereotactic body radiotherapy

Abbreviations: quantitative imaging biomarker (QIB), diffusion weighted imaging (DWI), single-shot echo-planar imaging (SS-EPI), magnetic resonance imaging (MRI), magnetic resonance (MR), apparent diffusion coefficient (ADC), dynamic contrast-enhanced (DCE), field of view (FOV), fast exchange limit (FXL), fast exchange regime (FXR), extravascular extracellular space (EES), echo time (TE), intracellular space (ICS), shutter-speed model (SSM), pancreatic ductal adenocarcinoma (PDAC), repetition time (TR), region-of-interest (ROI), stereotactic body radiotherapy (SBRT), treatment (TX), freedom from local progression (FFLP)

ABSTRACT

We aimed to assess longitudinal changes in quantitative imaging metric values obtained from diffusion-weighted (DW-) and dynamic contrast-enhanced magnetic resonance imaging (DCE)-MRI at pre-treatment (TX [0]), immediately after the first fraction of stereotactic body radiotherapy (D1-TX[1]), and 6 weeks post-TX (Post-TX[2]) in patients with pancreatic ductal adenocarcinoma. Ten enrolled patients (n = 10) underwent DW- and DCE-MRI examinations on a 3.0 T scanner. The apparent diffusion coefficient, ADC (mm^2/s), was derived from DW imaging data using a monoexponential model. The tissue relaxation rate, R_{1t}, time-course data were fitted with a shutter-speed model, which provides estimates of the volume transfer constant, K^{trans} (min^{-1}), extravascular extracellular volume fraction, v_e, and mean lifetime of intracellular water protons, τ_i (seconds). Wilcoxon rank-sum test compared the mean values, standard deviation, skewness, kurtosis, and relative percentage (r, %) changes (Δ) in ADC, K^{trans}, v_e, and τ_i values between the magnetic resonance examinations. $rADC_{\Delta 2-0}$ values were significantly greater than $rADC_{\Delta 1-0}$ values ($P = .009$). $rK^{trans}{}_{\Delta 2-0}$ values were significantly lower than $rK^{trans}{}_{\Delta 1-0}$ values ($P = .048$). $rv_{e\Delta 2-1}$ and $rv_{e\Delta 2-0}$ values were significantly different ($P = .016$). $r\tau_{i\Delta 2-1}$ values were significantly lower than $r\tau_{i\Delta 2-0}$ values ($P = .008$). For group comparison, the pre-TX mean and kurtosis of ADC ($P = .18$ and $P = .14$), skewness and kurtosis of K^{trans} values ($P = .14$ for both) showed a leaning toward significant difference between patients who experienced local control (n = 2) and failed early (n = 4). DW- and DCE-MRI-derived quantitative metrics could be useful biomarkers to evaluate longitudinal changes to stereotactic body radiotherapy in patients with pancreatic ductal adenocarcinoma.

INTRODUCTION

Pancreatic cancer is the fourth leading cause of cancer-related death in the United States (1). Pancreatic ductal adenocarcinoma (PDAC) is an aggressive disease with poor outcomes, especially for patients who are unable to undergo curative resection (2). PDAC is characterized by complex microarchitecture, dense fibroblastic stroma, and heterogeneous vascularization, which creates considerable challenges for therapy planning and response assessment (3, 4). Stereotactic body radiation therapy (SBRT) has emerged as an important treatment modality for patients with the localized unresectable disease (5). It is associated with similar survival compared with conventionally fractionated RT for locally advanced pancreas cancer (6) and is a promising technology for further dose escalation (7). Biomarkers of early response could facilitate adaptive replanning of SBRT and help inform post-SBRT management (8).

The quantitative imaging metrics derived from diffusion-weighted (DW) and dynamic contrast-enhanced (DCE)-MRI are emerging as surrogate biomarkers in differentiating between

ISSN 2379-1381 https://doi.org/10.18383/j.tom.2020.00015

normal pancreatic parenchyma and pancreatic tumors, as well as in assessing treatment response in PDAC (9–11). The utility of DW- and DCE-MRI techniques can be limited owing to the motion of abdominal organs, which can be minimized by either breath-hold (BH) or non-BH techniques, such as the respiratory-triggered technique (12–15).

DW-MRI describes the restriction/hindrance of translational motion of water molecules caused by tumor cellular structure in tissue. Water diffusion in the tumor is influenced by tissue composition, including cellularity, stroma content, and vascularization (16). The apparent diffusion coefficient (ADC) derived from the DW imaging signal, using monoexponential modeling, has shown promise for characterization, prognosis, and evaluation of treatment strategies in abdominal cancers (17). ADC is the surrogate biomarker for tumor cellularity because the macromolecular and microstructural changes occur at the cellular level earlier than anatomical changes during therapy (18). Previous studies have reported that mean ADC values of the normal pancreas were significantly higher than either pancreatic cancer or mass-forming pancreatitis (19, 20). Dalah et al. reported that the mean ADC values after neoadjuvant chemoradiation in PDAC correlated significantly with pathological responses (21). A recent study has reported that pre-treatment (TX) DW-MRI data could predict overall survival of patients with locally advanced pancreatic cancer treated using SBRT (11).

In contrast, DCE-MRI pharmacokinetic modeling confers measures of tumor microvascular physiology via pharmacokinetic modeling. Standard Tofts model provides estimates of K^{trans} and v_e (22). To quantify these parameters, changes in tissue water proton relaxation rate R_1 (ie, $\Delta R_1 = 1/\Delta T_1$) is assumed to be linearly related to contrast agent (CA) concentration in tissue, such that intercompartmental water exchange kinetics is at the fast exchange limit (FXL). When a significant amount of CA extravasates into extravascular extracellular space (EES), a large K^{trans}, transcytolemmal water exchange (ie, between intracellular space [ICS] and EES) drives out of the FXL into the fast exchange regime (FXR) (23). Landis et al. (23) showed the effects of transcytolemmal water exchange on estimates of T_1 longitudinal relaxation time in muscle tissue. The degree of ΔR_1 deviation from linearity depends on the magnetic resonance (MR) sequence parameters, in particular, on the flip angle (FA), the amount of CA extravasated into the EES, and the tissue under study (24, 25). FXR provides estimates of a mean lifetime of intracellular water protons, τ_i (ie, inverse of the water exchange rate, k_{ie}, from ICS to ESS), in addition to K^{trans} and v_e (26). K^{trans} and τ_i are surrogate biomarkers of tumor tissue perfusion/permeability and cellular metabolic activity, respectively (26, 27). The effects of transcytolemmal water exchange in estimates of T_1 have been investigated in DCE-MRI studies of breast cancer (26), head and neck cancer (28), and prostate cancer (29), but not in those of pancreatic cancer. Furthermore, both preclinical and clinical studies have shown utility for K^{trans} and τ_i as potential biomarkers, assessing tumors vasculature and cellular metabolism (30, 31).

DCE-MRI has been used to evaluate tumor vascular distribution and angiogenesis in the pancreas (32). K^{trans} has shown promise for monitoring therapeutic response in patients with PDAC (33, 34). The previous study has shown that the mean K^{trans} values in the responders' group were significantly higher than those in nonresponders group treated with gemcitabine-based chemotherapy in advanced PDAC (35). K^{trans} was significantly higher in tumors that showed a marked response than in those that did not when treated with chemotherapy and antiangiogenic therapy (33). Kim et al. reported an increase of K^{trans} in responsive tumors compared with a decrease of that in nonresponding tumors at 8 weeks post chemotherapy (34).

To the best of our knowledge, no study has used the combination of quantitative DW- and DCE-MRI in patients with PDAC longitudinally at multiple time points (ie, pre-[TX], after SBRT, and post-TX MRI). The purpose of the present prospective study was to assess longitudinal changes in quantitative imaging metric values obtained from DW- and DCE-MRI at pre-TX[0], immediately after the first fraction of SBRT (D1-TX[1]), and 6 weeks after SBRT (Post-TX[2]) in patients with PDAC.

MATERIALS AND METHODS

Patients

Our institutional review board approved this prospective longitudinal study, in compliance with the Health Insurance Portability and Accountability Act. Written informed consent was obtained from all eligible patients diagnosed with PDAC. Criteria for inclusion in the study required patients to be 18 years or older and with a diagnosis of PDAC, to be treated with SBRT. SBRT application followed a 3-fraction dose-escalation protocol with single fractions of 9–11Gy and total doses of 27–33 Gy and was given within 7 days. Ten patients (6 male and 4 female; median age, 64 years; range, 52–70 years) were enrolled and underwent MRI examinations. Figure 1 illustrates the timeline of longitudinal MRI examinations. MRI examinations were performed at pre-TX[0], immediately after the first fraction of SBRT (<90 minutes), D1-TX[1], and 6 weeks after SBRT (post-

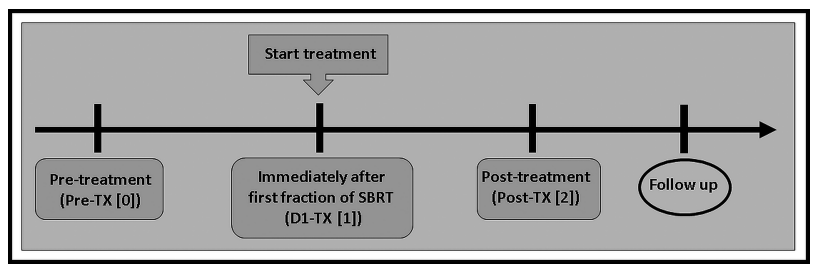

Figure 1. Timeline of magnetic resonance imaging examinations. Immediately after the first fraction of stereotactic body radiotherapy (SBRT), D1-treatment (TX) [1], was performed within 1–4 weeks from pre-TX[0], and post-TX[2] was performed 6-weeks after SBRT.

TX[2]). The D1-TX[1] and post-TX[2] MRI examinations were performed within 1–4 weeks and 8–12 weeks from the pre-TX[0] week, respectively. The accrual period for this study was from February 2016 to August 2018, and the summary of patients' characteristics is given in Table 1.

After SBRT, patients were evaluated every 3–6 months for the first 2 years, every 6 months up to 5 years and yearly thereafter. Patients were assessed for 12-month local control using standard clinical follow-up data including radiographic imaging. Out of 10, only 6 patients were evaluable. Two patients (n = 2) were alive at 12 months with no local progression and 4 patients (n = 4) had local progression within 12 months. Four patients were excluded from the above dichotomization who were either patients who died within 12 months with no evidence for local progression (n = 3) or patient (n = 1) who had surgery. The 3 patients who died within a couple of months after SBRT were excluded because we had no way of ascertaining whether these patients would have progressed shortly thereafter if they had remained alive a little longer. The follow-up time for freedom from local progression ranged from 2.5 to 33 months.

MRI Data Acquisition

All Pre-TX[0], D1-TX[1], and Post-TX[2] MR examinations were performed on a 3 T MR scanner (Philips Ingenia, Philips Healthcare, The Netherlands) using an integrated anterior–posterior dStream Torso coil. The standard T2-weighted (T2w) and T1-weighted (T1w) MR acquisition multiplanar (axial, coronal, and sagittal) were acquired under breath-hold. 2D T2-images were acquired using a fat-suppressed, fast spin-echo sequence with repetition time (TR) = 1250 milliseconds, echo time (TE) = 80 milliseconds, number of averages (NA) = 1, matrix size = 284 × 232 reconstructed to 256 × 256, slice thickness = 7 mm, slice spacing = 7 mm, field of view (FOV) = 30–35 cm, and number of slices (NS) = 24. The pre- and postcontrast 3D T1w images were acquired with TR = 3.01 milliseconds, TE = 1.41 milliseconds, NA = 1, slice thickness = 8 mm, slice spacing = 4 mm, matrix size = 196 × 194 reconstructed to 256 × 256, FOV = 30–35 cm, NS = 60. Multiple b-value DW-MRI and DCE-MRI acquisitions followed standard T1w and T2 w method.

Table 1. Patient Characteristics

Characteristics	Number (%)
Age, median (range), years	65 (52–70)
Sex	
Male	6 (60)
Female	4 (40)
Tumor location	
Head	5 (50)
Body	5 (50)
Pre-chemo tumor size, median (range), cm	5 (2.4–11.0)
Stage	
III	10 (100)
CA19-9, median (range), U/mL	48 (19–353)
Induction chemotherapy, median (range), months	4.4 (2.3–5.7)
FOLFIRINOX	8 (80)
Gemcitabine/nab-Paclitaxel	1 (10)
Both	1 (10)

Abbreviation: FOLFIRINOX: fluorouracil, leucovorin, irinotecan, and oxaliplatin.

DWI Data Acquisition

DW images were acquired using a single-shot echo-planar imaging (SS-EPI) sequence performed with 2 b-values of 0 and 500 s/mm^2 using a navigator triggered with the following MR parameters: TR = 3000 milliseconds, TE = 54 milliseconds (minimum), FOV = 30–35 cm, NS = 10–12, slice thickness = 6 mm, slice spacing = 6 mm, NA = 2 for b = 0 s/mm^2 and NA = 6 for b = 500 s/mm^2, and matrix = 132 × 130 (interpolated to 256 × 256). The total DWI acquisition time was ≤4 minutes.

DCE Data Acquisition

For generating the precontrast T1 (ie, T_{10}) maps, T1w images were acquired using the fast 3D T1w spoiled gradient recalled echo (SPGR) sequence with multiple FAs of 5°, 15°, and 30°. The DCE data acquisition scheme is shown in Figure 4B. Other acquisition MR parameters were as follows: TR/TE = 5.6 / 2.3 milliseconds, acquisition matrix = 231 × 116 reconstructed to matrix = 256 × 256 by zero-filling, FOV = 30–35 cm, slice thickness = 6 mm, slice spacing = 6 mm, and NS = 10–12. T1w dynamic series data were acquired for 20 phases with FA = 15° and other MR parameters, as mentioned above. After acquiring 3–4 precontrast images, a bolus of 0.1 mmol/kg Gd-based CA, used in clinical practice, was delivered through an antecubital vein catheter at 2 cc/s, followed by a 20-mL saline flush using an MR-compatible programmable power injector (Spectris; Medrad, Indianola, PA). DCE-MRI data were acquired with a series of multiple breath-holds. In the clinical setting, patients were requested by the technologist to hold their breath for ∼15 seconds followed by a ∼5-second break; the process was repeated multiple times for ≤5 minutes.

DW-MRI Data Analysis

The DW signal intensity data were fitted to a monoexponential model as follows (36):

$$S_b = S_0 e^{-bADC}, \quad [1]$$

where S_b and S_0 are the signal intensities with and without diffusion weighting, b is the diffusion-weighting factor (s/mm^2), and ADC is the apparent diffusion coefficient (mm^2/s).

DCE-MRI Pharmacokinetic Analysis

The signal intensity for T1w DCE acquired from a SPGR sequence is given by the following equation (37):

$$S(t) = \frac{M_0 \sin(\theta) e^{-\mathrm{TE}R_2^*(t)} \left(1 - e^{-\mathrm{TR}R_1(t)}\right)}{\left(1 - \cos(\theta) e^{-\mathrm{TR}R_1(t)}\right)}, \quad [2]$$

where $S(t)$ is the signal intensity at time t, M_0 is the equilibrium magnetization of the protons, θ is the FA, TR is repetition time, and TE is echo time. R_1(t) (R_1(t) = 1/$T1$(t)) [sec^{-1}] and $R_2^*(t)$

($R_2^*(t) = 1/T^*_2(t)$) [sec^{-1}] are the time-courses of longitudinal and transverse relaxation rate constants, respectively.

The $R_{1t}(t)$ can be derived from equation [2] when setting $e^{-TER_2^*(t)} \approx 1$ for $TE \ll T2^*$, and is given by the following equation:

$$R_{1t}(t) = \frac{1}{TR}\ln\left(\frac{1-\left(\frac{S(t)\cos(\theta)}{M_0\sin(\theta)}\right)}{1-\left(\frac{S(t)}{M_0\sin(\theta)}\right)}\right). \quad [3]$$

For the FXL, the time-course of tissue water proton relaxation rate, $R_{1t}(t)$, after CA administration, is expressed by the following equation (22):

$$R_{1t}(t) = R_{10} + r_1 C_t(t) \rightarrow \Delta R_{1t}(t) = R_{1t} - R_{10} = r_1 C_t(t), \quad [4]$$

where R_{10} and ΔR_{1t} (t) are the precontrast and change in tissue water relaxation rate R_1 time-course respectively, r_1 [$(mM)^{-1}s^{-1}$] is the CA longitudinal relaxivity, and $C_t(t)$ is the time-course of CA concentration in tissue.

The time-course of tissue CA concentration, $C_t(t)$, based on the standard Tofts model is given by the following equation (22):

$$C_t(t) = K^{trans}\int_0^t e^{-k_{ep}(t-\tau)}C_p(\tau)d\tau \quad [5]$$

where, K^{trans} (min^{-1}) is the volume transfer constant of CA, $C_p(\tau)$ is the time-course of plasma CA concentration (also called the arterial input function), $k_{ep} = \frac{K^{trans}}{v_e}$ is the transport rate constant of CA from EES to vascular space, and v_e is the EES volume fraction. The CA concentration in EES is calculated as follows: $C_e(t) = \frac{C_t(t)}{v_e}$.

FXL approximation may lead to significant errors in estimates of $C_t(t)$ when a large amount of CA extravasates into EES, such that FXL departs to FXR (also called SSM), in which the net rate of water exchange across cell membrane is: $k_c = k_{ie} + k_{ei} \approx |R_{1i} - R_{1e}|$). The k_{ie} ($k_{ie} = 1/\tau_i$) and k_{ei} are the rates of water exchange from ICS to EES and vice versa, and R_{1i} and R_{1e} are the longitudinal relaxation rates of ICS and EES, respectively.

To account for the effects of transcytolemmal water exchange in estimates of $C_t(t)$, the Bloch McConnell's equations for ICS and EES can be solved for negligible vascular space, v_p (23, 38). One of the solutions of the exchange matrix equation yields an observable relaxation rate, R_{1t}, which is given by equation [6] and the time-course of R_{1t} data fitted with SSM provides estimates of K^{trans} and v_e, and τ_i.

$$R_{1t}(t) = \frac{1}{2}[(R_{1i} + k_{ie} + R_{10e} + r_1 C_e(t) + k_{ei}) - \sqrt{(R_{1i} + k_{ie} - R_{10e} - r_1 C_e(t) - k_{ie})^2 + 4k_{ie}k_{ei}}], \quad [6]$$

where R_{10e} is the precontrast relaxation rate of EES in the absence of exchange.

Regions of Interest Analysis

Regions of interest (ROIs) were manually delineated on tumors in both the DWI images (b = 0 s/mm^2), and T1w DCE images, on late phases of the dynamic series, based on reference anatomical T2w/T1w images. Experienced abdominal radiologists and radiation oncologists contoured ROI's using ImageJ and ITK-SNAP (39, 40). DW signal data obtained from the ROIs were fitted on a voxel-by-voxel basis using a monoexponential model (equation [1]) to calculate the ADC (mm^2/s). The multiple FA T1w voxelwise signal data were fitted (equation [2]) to calculate the T_{10} and M_0 as detailed elsewhere (41). The R_{1t} time-course data (equation [3]) was fitted with SSM (equation [6]) for a given CA relaxivity of r_1 = 4.0 $(mM)^{-1}s^{-1}$ (26). The parametric maps of ADC, K^{trans}, ν_e, and τ_i were generated on a voxelwise basis to display the extent of the PDAC lesion. Model-fitting used a nonlinear least-squares algorithm that minimizes the sum of squared errors (SSEs) between model fit and data, as detailed elsewhere (42). Estimates of SSM metrics values were bounded as follows: $K^{trans} \in [0, 5]$ (min^{-1}), $v_e \in [0, 1]$, and $\tau_i \in [0, 2]$ (seconds). Arterial input function was extracted from the abdominal aorta, as described elsewhere (34).

The image registration method implemented in Elastix was used for the time-course of DCE data to minimize any potential misalignment in DCE-MRI as detailed elsewhere (43, 44).

The quantitative value of each metric extracted from analyses was reported as mean, standard deviation (SD), skewness, and kurtosis. All DW- and DCE-MRI image post-processing and quantitative metrics map generation were performed using in-house-developed software entitled MRI-QAMPER (MRI Quantitative Analysis of Multi-Parametric Evaluation Routines) (45).

A relative percentage change (r, %) in the quantitative metric value, X, between the longitudinal MR exams (ie, pre-TX[0], D1-TX[1], and post-TX[2]) was calculated as follows:

$$rX_{\Delta j-i}(\%) = \frac{X_j - X_i}{X_i} \times 100 \quad [7]$$

For simplicity in equation [7], Δ_{j-i} ($j = 1,2$ and $i = 0,1$) is described as follows: Δ_{1-0} = (D1-TX[1] − Pre-TX[0]), Δ_{2-0} = (Post-TX[2] − Pre-TX[0]), and Δ_{2-1} = (Post-TX[2] − D1-TX[1]).

Statistical Analysis

Wilcoxon rank-sum test (WSRT) was performed to compare the mean values of ADC, K^{trans}, v_e, and τ_i between the longitudinal MR examinations (ie, pre-TX[0], D1-TX[1], and post-TX[2]), and to compare their relative percentage (r, %) changes (Δ) between the longitudinal MR examinations. To compare the mean, SD, skewness, and kurtosis values of these metrics between the patients who showed local control and early failure, WRST test was used. All statistical calculations were conducted in R (46). For the correlation of MRI metrics with clinical outcomes, patients were dichotomized into binary clinical endpoints for local control at 12 months. Local control was defined using standard clinical follow-up and radiographic progression by RECIST 1.1 imaging criteria. A P-value $< .05$ was considered statistically significant.

RESULTS

In total, 27 MRI examinations (N = 27) from 10 patients with PDAC, including pre-TX[0] (N = 10), D1-TX[1] (N = 8), and post-

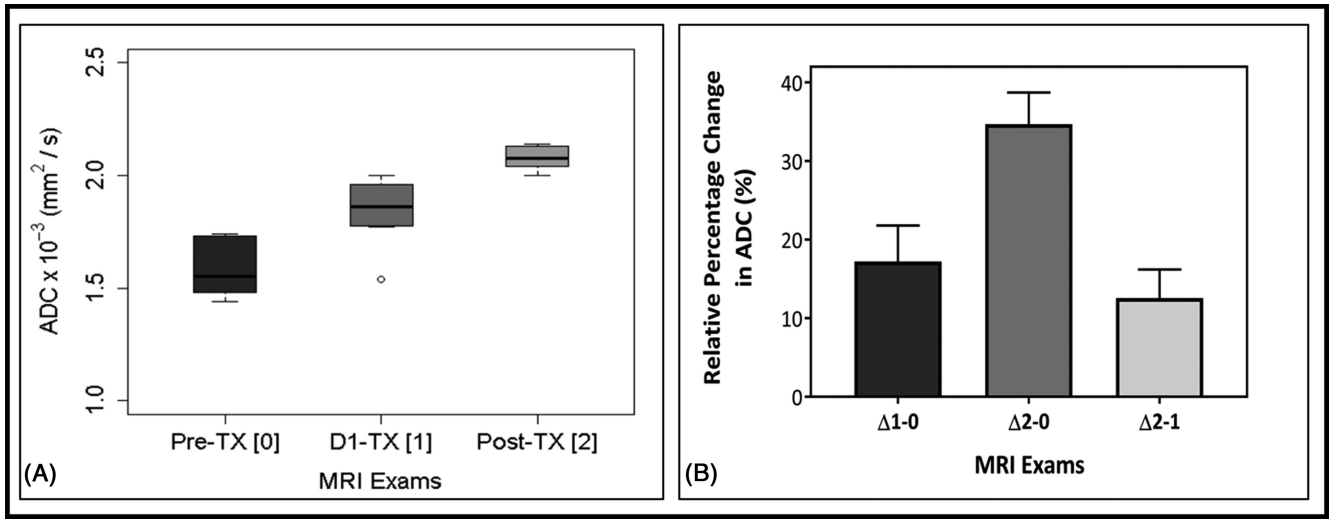

Figure 2. Box and whisker plot comparing mean apparent diffusion coefficient (ADC) values obtained from patients with pancreatic ductal adenocarcinoma (PDAC) at the longitudinal magnetic resonance examinations: pre-treatment (TX[0]), after the first fraction of stereotactic body radiotherapy, D1-TX[1], and post-TX[2]. ADC value showed a significant difference between these MRI examinations ($P < .05$). Boxes represent the interquartile range, whiskers represent the range of all values, and the horizontal line within the box is the median value. Open circles represent the outliers (A). Bar plots exhibit the longitudinal relative percentage changes in ADC values, and rΔADC (%) showed significant differences between MRI examinations ($P < .05$). Error bars indicate the standard error of the mean (B).

TX[2]) (N = 9), were successfully performed. Five out of 27 DW-MRI examinations were excluded owing to either poor signal-to-noise (n = 4) or total tumor volume was not fully captured (n = 1). One out of 27 DCE-MRI examinations (n = 1) was excluded from analysis, in which the total tumor volume was not fully captured. Tumors were located in the head (n = 5) and body (n = 5) of the pancreas. The mean tumor size (mean ± SD) was 5.15 ± 2.43 cm at pre-TX[0] in patients with PDAC. Local control and early failure tumor sizes in these patients were 4.20 ± 0.28 cm and 5.55 ± 2.56 cm, respectively.

DW-MRI

Figure 2A box and whisker plot display mean ADC values of the longitudinal MR examinations (ie, pre-TX[0], D1-TX[1], and post-TX[2]). Mean ADC values increased significantly at post-TX[2] ($2.08 \pm 0.06 \times 10^{-3}$ [mm^2/s]) than those of D1-TX[1] ($1.84 \pm 0.16 \times 10^{-3}$ [mm^2/s], $P = .003$) and pre-TX[0] ($1.58 \pm 0.13 \times 10^{-3}$ [mm^2/s], $P < .0001$). Mean ADC values at D1-TX[1] were significantly higher than those at pre-TX[0] ($P = .002$). Table 2 summarizes ADC values (mean ± SD) at pre-TX[1], D1-TX[1], and post-TX[2] MR examinations. The number of patients at pre-TX[0], D1-TX[1], and post-TX[2] MR examinations was n = 9, n = 7, and n = 6, respectively.

Figure 2B displays a bar graph of the relative percentage (r, %) changes (Δ) in ADC values between the longitudinal MR examinations (ie, $rADC_{\Delta 1\text{-}0}$, $rADC_{\Delta 2\text{-}0}$, and $rADC_{\Delta 2\text{-}1}$) in patients with PDAC. The changes (mean ± SD) in $rADC_{\Delta 1\text{-}0}$, $rADC_{\Delta 2\text{-}0}$, and $rADC_{\Delta 2\text{-}1}$ were 17% ± 11%, 34% ± 10%, and 13% ± 7%,

Table 2. DWI- and DCE-MRI-Derived Quantitative Metrics

Model	Parameter	Pre-TX	D1-TX	Post-TX	*P*-Value
DWI	ADC × 10^{-3} (mm^2/s)	1.58 ± 0.13	1.84 ± 0.16	2.08 ± 0.06	.002 (D1-TX vs Pre-TX) <.0001 (Post-TX vs Pre-TX) .003 (Post-TX vs D1-TX)
DCE-SSM	K^{trans} (min^{-1})	0.50 ± 0.26	0.90 ± 0.37	0.61 ± 0.24	.011 (D1-TX vs Pre-TX) .183 (Post-TX vs Pre-TX) .039 (Post-TX vs D1-TX)
	v_e	0.34 ± 0.14	0.39 ± 0.13	0.48 ± 0.18	.20 (D1-TX vs Pre-TX) .04 (Post-TX vs Pre-TX) .11 (Post-TX vs D1-TX)
	τ_i (seconds)	0.62 ± 0.18	0.75 ± 0.12	0.48 ± 0.18	.045 (D1-TX vs Pre-TX) .065 (Post-TX vs Pre-TX) .001 (Post-TX vs D1-TX)

respectively. $rADC_{\Delta 2\text{-}0}$ and $rADC_{\Delta 1\text{-}0}$ values were significantly different ($P = .009$), whereas $rADC_{\Delta 2\text{-}1}$ and $rADC_{\Delta 1\text{-}0}$ were not significantly different ($P = .22$). $rADC_{\Delta 2\text{-}1}$ and $rADC_{\Delta 2\text{-}0}$ showed significantly different ($P = .002$). The number of patients for $rADC_{\Delta 1\text{-}0}$, $rADC_{\Delta 2\text{-}0}$, and $rADC_{\Delta 2\text{-}1}$ was n = 6, n = 6, and n = 4, respectively.

Figure 3 exhibits the representative pre-TX[0] and D1-TX[1] DW images (b = 0 s/mm^2) obtained from a patient with PDAC (61 years, female) who showed a local control. ROI at pre-TX[0] and D1-TX[1] are outlined in yellow. ADC maps are overlaid on the DW image (b = 0 s/mm^2) at pre-TX[0] and D1-TX[1]. The tumor cellular heterogeneity across the ROI can be seen in both pre- and D1-TX and higher ADC values predominating at D1-TX[1].

For group comparison as an exploratory analysis at pre-TX[0], 6 patients qualified for local control at 12 months, 2 patients had local control of disease at last clinical follow-up, and 4 patients showed evidence for local progression within 12 months after treatment. Pre-TX[0] mean ADC value was 7% higher in the local control group patients than in patients who failed early ($1.60 \pm 0.17 \times 10^{-3}$ [mm^2/s] vs $1.50 \pm 0.05 \times 10^{-3}$ [mm^2/s]). Mean values of ADC showed a leaning toward significant difference ($P = .18$), and a similar trend was seen in ADC kurtosis values ($P = .14$) between these 2 groups at pre-TX[0]. As a note, 1 patient out of 4 patients who failed early was excluded as tumor ROI was not fully captured at pre-TX[0].

DCE-MRI

Figure 4A shows the plot of tissue water protons longitudinal relaxation rate, R_{1t}, time-course data obtained from the 1 enhancing voxel fitted with SSM. ROIs are outlined in yellow at pre-TX[0] and D1-TX[1] (Figure 7). The open circle corresponds to R_{1t} data (black), and the solid line (black) to the SSM fit. An arterial input function extracted from the abdominal aorta is outlined in the red circle at D1-TX[1] (Figure 7). A plot of plasma CA concentration, $C_p(\tau)$, time-course data (inset). The SSM fitting yielded K^{trans} = 0.36 (min^{-1}), v_e = 0.23, and τ_i = 0.51 (seconds). Figure 4B exhibits the representative DCE data acquisition schema.

Figure 5 shows the box and whisker plot that displays the distribution of mean K^{trans}, v_e, and τ_i values for the longitudinal MR examinations (pre-TX[0], D1-TX[1] and post-TX[2]). Mean K^{trans} values (0.90 ± 0.37 [min^{-1}] at D1-TX[1] were significantly higher than those at pre-TX[0] (0.50 ± 0.26 [min^{-1}], $P = .011$) and at post-TX[2] (0.61 ± 0.24 [min^{-1}], $P = .039$). Mean K^{trans} values at post-TX[2] showed a higher trend than those at pre-TX[0] but were not significantly different ($P = .18$). Mean v_e values at post-TX[2] increased significantly from those at pre-TX[0] (0.48 ± 0.18 vs 0.34 ± 0.14, $P = .042$). Mean v_e values at D1-TX[1] (0.39 ± 0.10) and at pre-TX[0], as well as at post-TX[2] and at D1-TX[1], were not significantly different ($P > .05$). Mean τ_i values at D1-TX[0] (0.75 ± 0.12 [seconds]) were significantly higher than those of pre-TX[0] (0.62 ± 0.18 [seconds], $P = .045$) and post-TX[2] MR examination (0.48 ± 0.18 [seconds], $P = .001$). Mean τ_i values at post-TX[2] showed a trend toward being significantly lower than those at pre-TX[0] ($P = .065$). Table 2 shows the summary of K^{trans}, v_e, and τ_i values obtained from SSM at pre-TX[0], D1-TX[1], and post-TX[2] MR examinations. The number of patients at pre-TX[0], D1-TX[1], and post-TX[2] was n= 9, n= 8 and n = 9, respectively.

Figure 6 is a bar graph that displays the relative percentage (r, %) changes (Δ) in SSM-derived metric values K^{trans} ($rK^{trans}_{\Delta 1\text{-}0}$, $rK^{trans}_{\Delta 2\text{-}0}$, and $rK^{trans}_{\Delta 2\text{-}1}$), v_e ($rv_{e\Delta 1\text{-}0}$, $rv_{e\,\Delta 2\text{-}0}$, and $rv_{e\,\Delta 2\text{-}1}$), and τ_i ($r\tau_{i\Delta 1\text{-}0}$, $r\tau_{i\,\Delta 2\text{-}0}$, and $r\tau_{i\,\Delta 2\text{-}1}$) between the longitudinal MR examinations. The number of patients at pre-TX[0], D1-TX[1], and post-TX[2] was n= 9, n= 8, and n = 9, respectively.

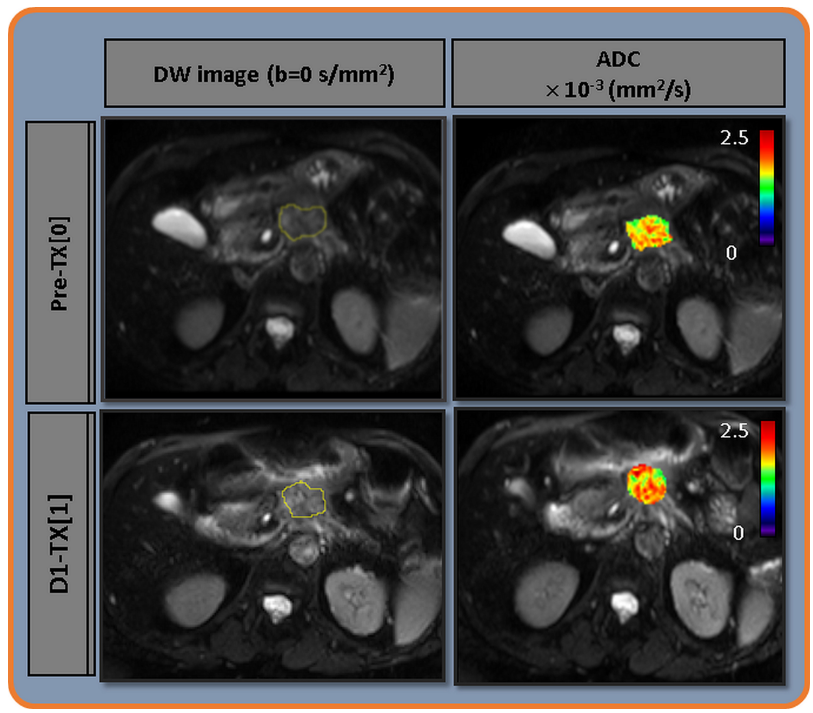

Figure 3. Left: Representative diffusion-weighted (DW) images (b = 0 [s/mm^2]) obtained from a patient with PDAC who showed a local control (61 years, female) at pre-treatment (TX[0]) and immediately after the first fraction of stereotactic body radiotherapy, D1-TX[1]. Regions of interest are outlined in yellow. Right: ADC maps overlaid on DW image (b = 0 [s/mm^2]) at pre-TX[0] and D1-TX[1]. An increase in ADC value at post-TX[2] is evident.

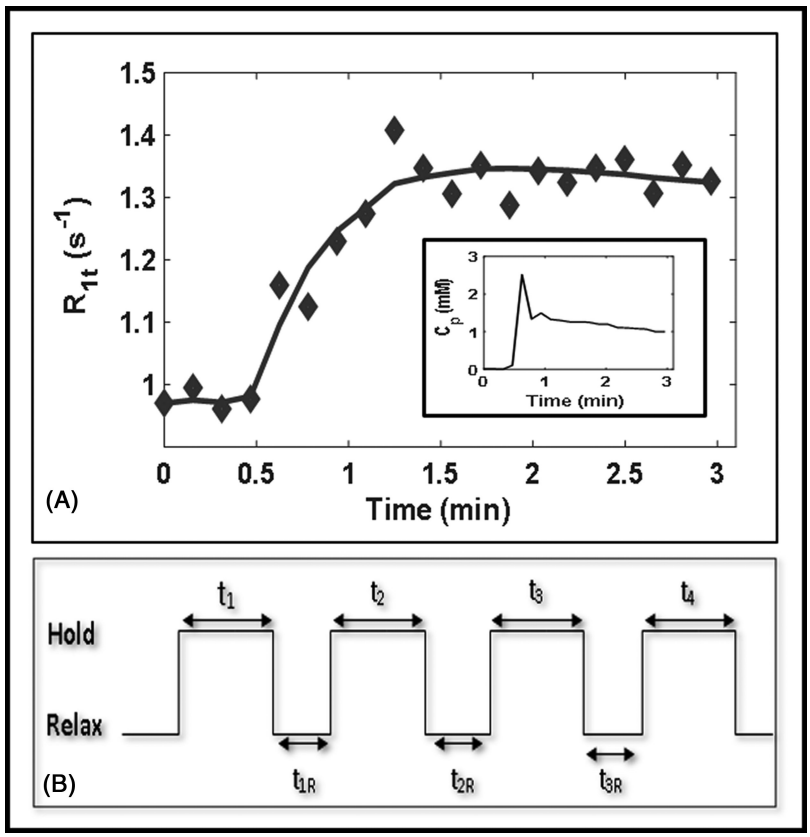

Figure 4. Plot of the representative longitudinal relaxation rate, $R_{1t}(t)$, time-course data obtained from 1 enhancing pixel fitted with the shutter-speed model. Regions of interest are outlined in yellow at pre-TX[0] and immediately after the first fraction of stereotactic body radiotherapy, D1-TX[1]. Inset: The plasma contrast agent concentration, C_p, data plot extracted from the aorta, which is outlined in the red circle at D1-TX[1] (A). Representative dynamic contrast-enhanced data acquisition schema (B).

The changes (mean ± SD) in K^{trans} (ie, $rK^{trans}_{\Delta 1\text{-}0}$ and $rK^{trans}_{\Delta 2\text{-}0}$) values were 91% ± 104% and 33% ± 70%, respectively, and were significantly different ($P = .048$), whereas $rK^{trans}_{\Delta 2\text{-}1}$ decreased by −20% ± 42%, and showed a borderline significant difference from that of $rK^{trans}_{\Delta 1\text{-}0}$ ($P = .062$). The changes in $rK^{trans}_{\Delta 2\text{-}1}$ and $rK^{trans}_{\Delta 2\text{-}0}$ were not significantly different ($P = .35$).

The changes (mean ± SD) in v_e values (ie, $rv_{e\Delta 1\text{-}0}$ and $rv_{e\Delta 2\text{-}0}$, and $rv_{e\Delta 2\text{-}1}$) were 15% ± 38%, 51% ± 77%, and 37% ± 76%,

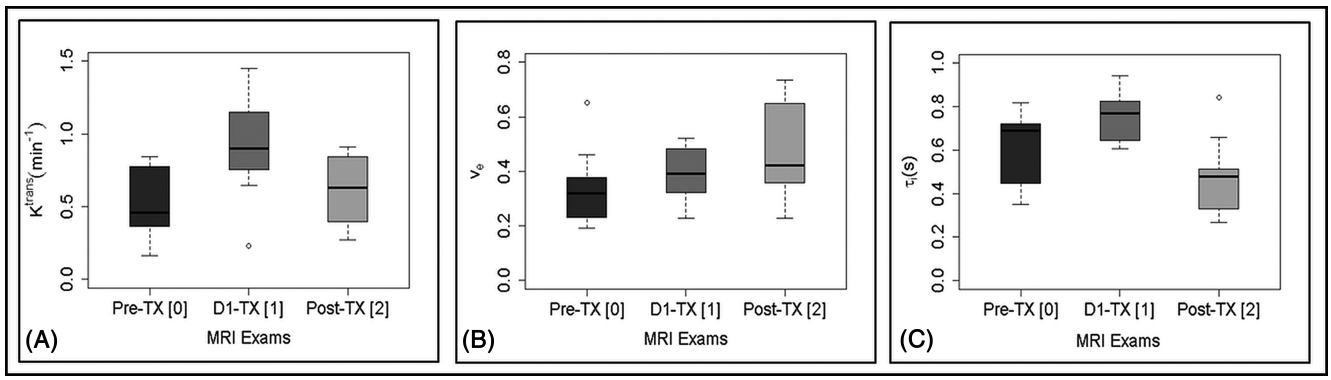

Figure 5. Box and whisker plots show quantitative metric mean values obtained with the shutter speed model in longitudinal MR examinations (ie, pre-treatment [TX 0], immediately after the first fraction of stereotactic body radiotherapy, D1-TX[1], and post-TX[2]). K^{trans} (min^{-1}) (A), v_e (B), and τ_i (seconds) (C). K^{trans} values at D1-TX were significantly higher than those at pre-TX ($P = .011$) and post-TX ($P = .039$). v_e values at pre-TX were significantly lower than those at post-TX ($P = .042$). D1-TX τ_i values were significantly higher than pre-TX ($P = .045$) and post-TX ($P = .001$) values. τ_i values at pre- and post-TX showed borderline significance ($P = .065$). Boxes represent the interquartile range, whiskers represent the range of all values, the horizontal line within the box is the median value, and the open circle represents the outliers. Moderate overlap of quantitative metric values is evident.

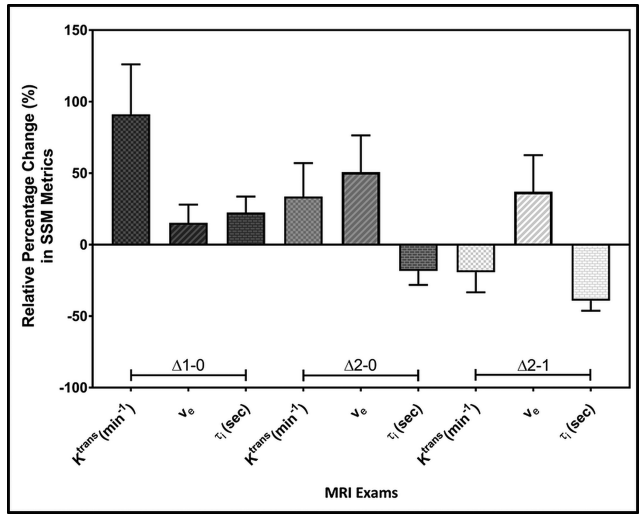

Figure 6. Bar plots display the relative percentage changes in mean K^{trans} (min^{-1}), v_e, and τ_i (seconds) values between longitudinal MR examinations (ie, pre-treatment (TX[0]), immediately after the first fraction of stereotactic body radiotherapy D1-TX[1], and post-TX[2]). $rK^{trans}_{\Delta 2\text{-}0}$ versus $rK^{trans}_{\Delta 1\text{-}0}$, $rv_{e\Delta 2\text{-}1}$ versus $rv_{e\Delta 2\text{-}0}$, $rv_{e\Delta 2\text{-}1}$ versus $rv_{e\Delta 2\text{-}0}$, and $r\tau_{i\Delta 2\text{-}1}$ versus $r\tau_{i2\text{-}0}$ exhibited significant differences ($P < .05$). Error bars indicate the standard error of the mean.

respectively. When comparing $rv_{e\Delta 2\text{-}1}$ versus $rv_{e\Delta 1\text{-}0}$ and $rv_{e\Delta 2\text{-}1}$ versus $rv_{e\Delta 1\text{-}0}$, these values showed a significant difference ($P = .037$ and $P = .016$, respectively).

The changes (mean ± SD) in $r\tau_{i\Delta 1\text{-}0}$ increased by 22% ± 33%, whereas $r\tau_{i\,\Delta 2\text{-}0}$ and $r\tau_{i\Delta 2\text{-}1}$ decreased by 18% ± 29%, and −39% ± 21%, respectively. $r\tau_{i\Delta 2\text{-}0}$ versus $r\tau_{i\Delta 1\text{-}0}$ and $r\tau_{i\Delta 2\text{-}1}$ versus $r\tau_{i\Delta 2\text{-}0}$ were significantly different ($P = .045$ and $P = .0085$, respectively), whereas $r\tau_{i\Delta 2\text{-}1}$ and $r\tau_{i\ \Delta 1\text{-}0}$ showed a difference trend but was not significant ($P = .12$).

Figure 7 exhibits representative pre-TX[0] and D1-TX[1] T1w images from a patient with PDAC (61 years, female) who showed a local control (left). Representative K^{trans}, v_e, and τ_i maps overlaid on the precontrast T1w images at pre-TX[0] and D1-TX[1] MR examinations (right). The elevated values of K^{trans}, v_e, and τ_i can be seen at D1-TX[1]. K^{trans} and τ_i maps show alternatively elevated and smaller values at pre-TX[0] and D1-TX[1], respectively.

In an exploratory analysis, 6 patients were evaluable for local control at 12 month, 2 patients had local control of disease at last clinical follow-up, and 4 patients showed evidence for local progression within 12 months after treatment for group comparison. At pre-TX[0], the mean K^{trans} value of the local control group was 56% smaller than that of patients who failed early (0.26 ± 0.14 vs 0.61 ± 0.35 [min^{-1}]). K^{trans} skewness and kurtosis values showed a leaning toward significant difference between 2 groups ($P = .14$). The mean v_e values of the 2 groups differed by 8% (0.33 ± 0.22 vs 0.37 ± 0.25), and the mean τ_i values differed by 5% (0.58 ± 0.24 vs 0.61 ± 0.14) for patients who experienced local control at last clinical follow-up versus patients who failed early.

DISCUSSION

To the best of our knowledge, this is the first preliminary longitudinal MR study (ie, pre-TX[0], immediately after the first fraction of SBRT (<90 minutes), D1-TX[1], and 6 weeks after SBRT (post-TX[2]) in PDAC that reports changes in metric values ADC (mm^2/s) and SSM DCE-derived metrics (ie, K^{trans} (min^{-1}), v_e, and τ_i (seconds). ADC, a marker of tissue water diffusion restriction and cellularity, K^{trans}, an index of vascular perfusion/permeability, and τ_i, a marker of metabolic activity of a cell, could provide useful quantitative, physiological, and functional information in patients with PDAC. The greatest changes in K^{trans} occurred immediately after the first fraction of SBRT, whereas τ_i showed a significant change at post-TX. ADC and v_e values showed the greatest change at the post-TX MRI examination. Even though the sample size for group comparison was small, we found differences in mean, skewness and/or kurtosis ADC, K^{trans}, v_e, and τ_i values between the patients who showed local control (n = 2) and early failure (n = 4) at pre-TX. ADC and SSM derived biomarkers could capture the longitudinal change in tumor physiology, which has a unique tumor microenvironment (ie, stroma-rich) in patients with PDAC.

SBRT is an emerging technology that has enabled dose escalation and has the potential to improve patient outcomes (4, 42) further. PDAC response to radiation has traditionally been assessed by measuring tumor size. However, these changes are slow to occur, and size measurements are further complicated by the irregular shape common to PDACs. Functional MR imaging, including DW- and DCE-MRI, can help assess the biological effects of therapy in tumor and surrounding normal tissue before changes in tumor size or normal organ architecture become visible. The DWI and DCE advanced quantitative imaging metrics can provide tumor characteristics (ie, cellularity, vascularity, and cellular metabolic activity) in response to the first dose of SBRT and could potentially enable biologically driven adaptive optimization of an SBRT plan. In addition, early post-SBRT biomarkers would help inform post-SBRT treatment decisions. Currently, options after SBRT include consideration of surgery, observation, and additional systemic therapy (5). Decisions regarding management are primarily based on anatomic imaging, which is notoriously flawed after chemoradiotherapy (47), or CA19-9 serum biomarker that may indicate a progression of the disease without differentiating between local or distant disease (48). Thus, early longitudinal changes in biomarkers for SBRT of PDAC would greatly add to clinical decision-making.

Diffusion of water molecules in pancreatic tissue is highly restricted owing to structural barriers, including cellularity, stroma content, and vascularization (18). A previous preclinical study reported that tumor cellularity is a prognostic feature and may be of predictive importance given the emergence of stroma-acting treatment approaches (49). Dalah et al. found a significant correlation between the change in ADC values before and after treatment and pathological treatment response in patients with PDAC following neoadjuvant chemoradiation (21).

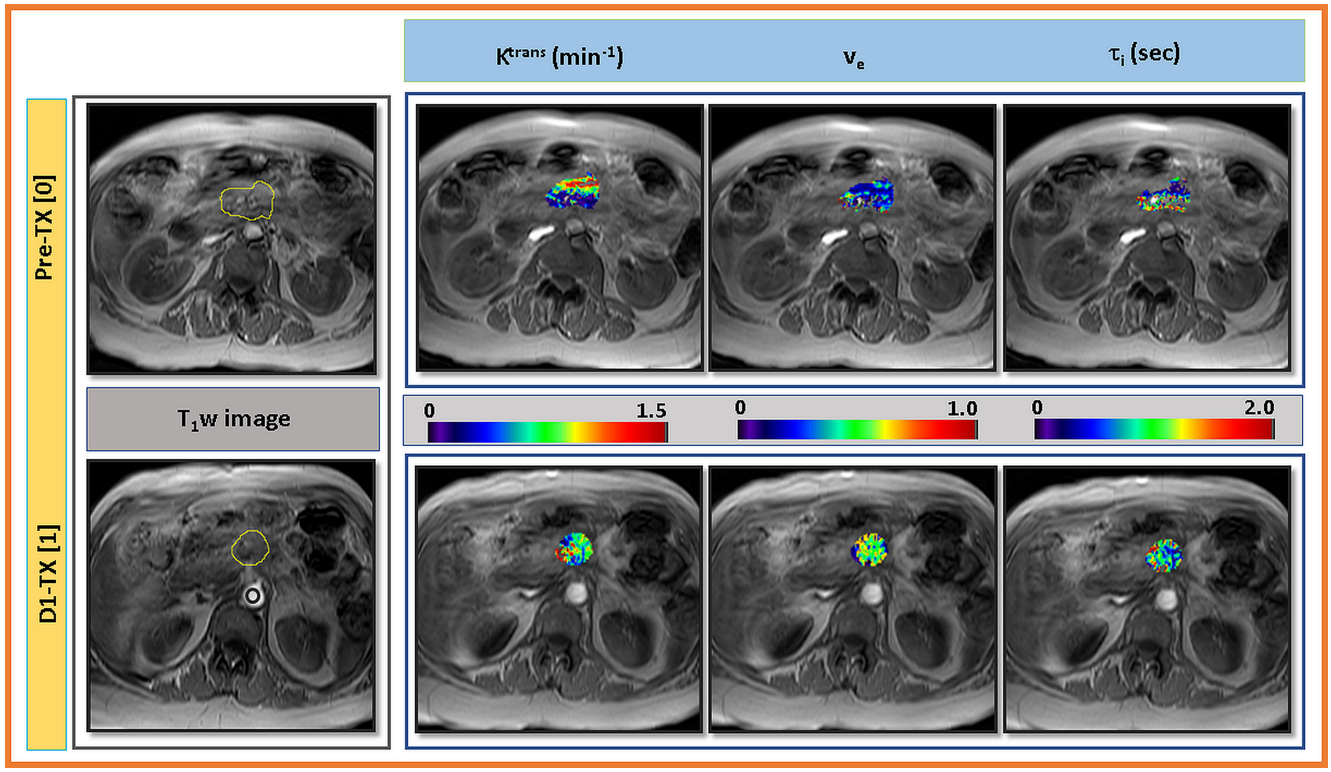

Figure 7. Left: Representative T1-weighted (T1w) images at pre-treatment (TX[0]) and immediately after the first fraction of stereotactic body radiotherapy, D1-TX[1], from a patient who showed a local control (61 years, female). ROIs were drawn on the pancreatic tumor (outlined in yellow color) and aorta (outlined in red circle) for the plasma contrast agent concentration, Cp. Right: Representative SSM-derived parametric maps of K^{trans}, v_e, and τ_i overlaid on T1w image at longitudinal MR examinations (ie, pre-TX[0] and D1-TX[1]). An increase in quantitative metrics value after the first fraction of SBRT is evident.

In the present study, the mean ADC value increased by 34% post-TX following successful SBRT treatment, indicating a significant loss of cell membrane integrity and cell density such that the geometrical arrangement has become more favorable for freely diffusing water molecules.

PDAC has an extraordinarily dense fibrous stroma that impedes tumor perfusion and delivery of anticancer drugs (3). Pretreatment K^{trans}, a marker of both perfusion and permeability, has been shown to predict response to antiangiogenic therapy in pancreatic tumors (33). Kim et al. reported that an increase in tumor perfusion correlates significantly with the chemotherapeutic response in PDAC, and these study findings were consistent with a preclinical study (50–52). The present study showed a significant increase in K^{trans} immediately after the first fraction of SBRT, which may be related to changes in the interstitial fluid pressure (53). Our finding is consistent with the CT perfusion imaging performed within 60 minutes of ablative radiotherapy, which revealed significant increases in blood flow and permeability (unpublished data). Earlier studies have reported that τ_i is inversely correlated with cell membrane ion-pump activity, which is considered a measure of mitochondrial metabolism and suggesting that τ_i might be a sensitive indicator of cellular energy turnover (27, 30, 31). τ_i is related to the mean transcytolemmal water permeability coefficient, P_W, and the size of the cell ($\approx P_w/r$) (31). τ_i obtained from the SSM analysis might be of particular interest to assess SBRT response in PDAC. Thus, a better understanding of the pathophysiology of pancreatic cancer is essential for mapping the tumor microenvironment and for establishing guidelines for therapy.

Group comparison at pre-TX[0] was performed for 6 patients between those who had local control (n = 2) and those who failed early (n = 4). The mean tumor size in patients who showed local control was 24% smaller than that in patients of early failure. The summary statistics, such as SD, skewness, and kurtosis, provide heterogeneity of tumors and degree of asymmetry of the distribution of the quantitative metric values. In the present study, kurtosis of ADC and skewness and kurtosis of K^{trans} indicated differences in tumor microenvironment between patients who experienced local control and failed early at pre-TX[0]. As a note, ADC is related to tumor cellularity, whereas K^{trans}, an index of tumor blood flow and vessel permeability, is associated with the degree of tumor tissue vascularization, and τ_i is an index of cellular metabolism. SSM-derived metrics K^{trans} and τ_i have shown promise to predict overall survival in head and neck and breast cancers (31, 54). However, the increase or decrease of these quantitative metrics after therapy could depend on the tumor

physiology and treatment modality (28, 29). In this scenario, it is very critical to perform longitudinal DW- and DCE-MRI so that the treating physician can see the early pattern of changes in metric values and decide if additional therapy is needed in patients with PDAC who fail early to TX.

The main limitation of this prospective study was the small patient cohort, with short clinical follow-up precluding correlation with long-term response outcomes. However, preliminary results indicated significant differences in metric values for both DW- and DCE-MRI on longitudinal MRI follow-up and may serve as the basis for further validation studies with larger sample sizes. For DCE-MRI, B_1 inhomogeneity can influence estimates of K^{trans} if properly not accounted for in the analysis.

CONCLUSION

Quantitative imaging metrics derived from DW (ie, ADC) and SSM DCE-MRI (ie, K^{trans} and τ_i) performed longitudinally, pre-TX[0], immediately after the first fraction of SBRT (D1-TX[1]) and 6 weeks after SBRT (post-TX[2]) MRI examinations, show initial promise as early-response biomarkers for SBRT in patients with PDAC. Following appropriate validation, these measures could potentially enable improved adaptive planning of SBRT and help guide post-SBRT treatment decisions.

ACKNOWLEDGMENT

Equal Contribution: R.D., M.R., and R.P. contributed equally to this study.
We acknowledge funding from NIH U01 CA211205 and NIH/NCI Cancer Center Support Grant P30 CA008748.

Conflict of Interest: None reported.

Disclosures: No disclosures to report.

REFERENCES

1. Siegel RL, Miller KD, Jemal A. Cancer statistics, 2019. CA A Cancer J Clin. 2019;69:7–34.
2. Orth M, Metzger P, Gerum S, Mayerle J, Schneider G, Belka C, Schnurr M, Lauber K. Pancreatic ductal adenocarcinoma: biological hallmarks, current status, and future perspectives of combined modality treatment approaches. Radiat Oncol. 2019; 14:141.
3. Hidalgo M. Pancreatic cancer. N Engl J Med. 2010;362:1605–1617.
4. Koong AC, Le QT, Ho A, Fong B, Fisher G, Cho C, Ford J, Poen J, Gibbs IC, Mehta VK, Kee S, Trueblood W, Yang G, Bastidas JA. Phase I study of stereotactic radiosurgery in patients with locally advanced pancreatic cancer. Int J Radiat Oncol Biol Phys. 2004;58:1017–1021.
5. Trakul N, Koong AC, Chang DT. Stereotactic body radiotherapy in the treatment of pancreatic cancer. Semin Radiat Oncol. 2014;24:140–147.
6. Zhong J, Patel K, Switchenko J, Cassidy RJ, Hall WA, Gillespie T, Patel PR, Kooby D, Landry J. Outcomes for patients with locally advanced pancreatic adenocarcinoma treated with stereotactic body radiation therapy versus conventionally fractionated radiation. Cancer. 2017;123:3486–3493.
7. Krishnan S, Chadha AS, Suh Y, Chen H-C, Rao A, Das P, Minsky BD, Mahmood U, Delclos ME, Sawakuchi GO, Beddar S, Katz MH, Fleming JB, Javle MM, Varadhachary GR, Wolff RA, Crane CH. Focal radiation therapy dose escalation improves overall survival in locally advanced pancreatic cancer patients receiving induction chemotherapy and consolidative chemoradiation. Int J Radiat Oncol Biol Phys. 2016;94: 755–765.
8. Rosati LM, Herman JM. Role of stereotactic body radiotherapy in the treatment of elderly and poor performance status patients with pancreatic cancer. J Oncol Pract. 2017;13:157–166.
9. Nishiofuku H, Tanaka T, Marugami N, Sho M, Akahori T, Nakajima Y, Kichikawa K. Increased tumour ADC value during chemotherapy predicts improved survival in unresectable pancreatic cancer. Eur Radiol. 2016;26:1835–1842.
10. Kang KM, Lee JM, Shin C-I, Baek JH, Kim SH, Yoon JH, Han JK, Choi BI. Added value of diffusion-weighted imaging to MR cholangiopancreatography with unenhanced mr imaging for predicting malignancy or invasiveness of intraductal papillary mucinous neoplasm of the pancreas. J Magn Reson Imaging. 2013;38:555–563.
11. Zhang Y, Zhu X, Liu R, Wang X, Sun G, Song J, Lu J, Zhang H. Combination of pre-treatment DWI-signal intensity and S-1 treatment: a predictor of survival in patients with locally advanced pancreatic cancer receiving stereotactic body radiation therapy and sequential S-1. Transl Oncol. 2018;11:399–405.
12. Kartalis N, Lindholm TL, Aspelin P, Permert J, Albiin N. Diffusion-weighted magnetic resonance imaging of pancreas tumours. Eur Radiol. 2009;19:1981–1990.
13. Kim JH, Lee JM, Park JH, Kim SC, Joo I, Han JK, Choi BI. Solid pancreatic lesions: characterization by using timing bolus dynamic contrast-enhanced mr imaging assessment-a preliminary study. Radiology. 2013;266:185–196.
14. Yao X, Zeng M, Wang H, Sun F, Rao S, Ji Y. Evaluation of pancreatic cancer by multiple breath-hold dynamic contrast-enhanced magnetic resonance imaging at 3.0T. Eur J Radiol. 2012;81:e917–22.
15. Chen Y, Lee GR, Wright KL, Badve C, Nakamoto D, Yu A, Schluchter MD, Griswold MA, Seiberlich N, Gulani V. Free-breathing liver perfusion imaging using 3-dimensional through-time spiral generalized autocalibrating partially parallel acquisition acceleration. Invest Radiol. 2015;50:367–375.
16. Trajkovic-Arsic M, Heid I, Steiger K, Gupta A, Fingerle A, Wörner C, Teichmann N, Sengkwawoh-Lueong S, Wenzel P, Beer AJ, Esposito I, Braren R, Siveke JT. Apparent diffusion coefficient (ADC) predicts therapy response in pancreatic ductal adenocarcinoma. Sci Rep. 2017;7:17038.
17. Barral M, Taouli B, Guiu B, Koh D-M, Luciani A, Manfredi R, Vilgrain V, Hoeffel C, Kanematsu M, Soyer P. Diffusion-weighted MR imaging of the pancreas: current status and recommendations. Radiology. 2015;274:45–63.
18. De Robertis R, Tinazzi MP, Demozzi E, Dal CF, Bassi C, Pederzoli P, D'Onofrio M. Diffusion-weighted imaging of pancreatic cancer. World J Radiol. 2015;7:319–328.
19. Lee SS, Byun JH, Park BJ, Park SH, Kim N, Park B, Kim JK, Lee M-G. Quantitative analysis of diffusion-weighted magnetic resonance imaging of the pancreas: usefulness in characterizing solid pancreatic masses. J Magn Reson Imaging. 2008;28:928–936.
20. Fattahi R, Balci NC, Perman WH, Hsueh EC, Alkaade S, Havlioglu N, Burton FR. Pancreatic diffusion-weighted imaging (DWI): comparison between mass-forming focal pancreatitis (FP), pancreatic cancer (PC), and normal pancreas. J Magn Reson Imaging. 2009;29:350–356.
21. Dalah E, Erickson B, Oshima K, Schott D, Hall WA, Paulson E, Tai A, Knechtges P, Li XA. Correlation of ADC with pathological treatment response for radiation therapy of pancreatic cancer. Translati Oncol. 2018;11:391–398.
22. Tofts PS, Brix G, Buckley DL, Evelhoch JL, Henderson E, Knopp MV, Larsson HBW, Lee T-Y, Mayr NA, Parker GJM, Port RE, Taylor J, Weisskoff RM. Estimating kinetic parameters from dynamic contrast-enhanced T(1)-weighted MRI of a diffusable tracer: standardized quantities and symbols. J Magn Reson Imaging. 1999;10:223–232.
23. Landis CS, Li X, Telang FW, Molina PE, Palyka I, Vetek G, Springer CS. Equilibrium transcytolemmal water-exchange kinetics in skeletal muscle in vivo. Magn Reson Med. 1999;42:467–478.
24. Paudyal R, Poptani H, Cai K, Zhou R, Glickson JD. Impact of transvascular and cellular-interstitial water exchange on dynamic contrast-enhanced magnetic resonance imaging estimates of blood to tissue transfer constant and blood plasma volume. J Magn Reson Imaging. 2013;37:435–444.
25. Zhang J, Kim SG. Estimation of cellular-interstitial water exchange in dynamic contrast enhanced MRI using two flip angles. NMR Biomed. 2019;32.
26. Yankeelov TE, Lepage M, Chakravarthy A, Broome EE, Niermann KJ, Kelley MC, Meszoely I, Mayer IA, Herman CR, McManus K, Price RR, Gore JC. Integration of quantitative DCE-MRI and ADC mapping to monitor treatment response in human breast cancer: initial results. Magn Reson Imaging. 2007;25:1–13.
27. Zhang YJ, Poirier-Quinot M, Springer CS, Balschi JA. Active trans-plasma membrane water cycling in yeast is revealed by NMR. Biophys J. 2011;101:2833–2842.
28. Kim S, Loevner LA, Quon H, Kilger A, Sherman E, Weinstein G, Chalian A, Poptani H. Prediction of response to chemoradiation therapy in squamous cell carcinomas of the head and neck using dynamic contrast-enhanced MR imaging. AJNR Am J Neuroradiol. 2010;31:262–268.
29. Li X, Priest RA, Woodward WJ, Tagge IJ, Siddiqui F, Huang W, Rooney WD, Beer TM, Garzotto MG, Springer CS. Feasibility of shutter-speed DCE-MRI for improved prostate cancer detection. Magn Reson Med. 2013;69:171–178.
30. Nath K, Paudyal R, Nelson D, Pickup S, Zhou R, Leeper D, Heitjan D, Springer CS, Poptani H, Glickson JD. Acute changes in cellular-interstitial water exchange rate in

DB-1 Melanoma xenografts after Ionidamine administration as a marker of tumor energetics and ion transport. Proc Intl Soc Magn Reson Med. 2014.
31. Springer CS, Li X, Tudorica LA, Oh KY, Roy N, Chui SY-C, Naik AM, Holtorf ML, Afzal A, Rooney WD, Huang W. Intratumor mapping of intracellular water lifetime: metabolic images of breast cancer? NMR Biomed. 2014;27:760–773.
32. Ma C, Li YJ, Pan CS, Wang H, Wang J, Chen SY, Lu JP. High resolution diffusion weighted magnetic resonance imaging of the pancreas using reduced field of view single-shot echo-planar imaging at 3 T. Magn Reson Imaging. 2014;32:125–131.
33. Akisik MF, Sandrasegaran K, Bu G, Lin C, Hutchins GD, Chiorean EG. Pancreatic cancer: utility of dynamic contrast-enhanced MR imaging in assessment of antiangiogenic therapy. Radiology. 2010;256:441–449.
34. Kim H, Morgan DE, Schexnailder P, Navari RM, Williams GR, Bart Rose J, Li Y, Paluri R. Accurate therapeutic response assessment of pancreatic ductal adenocarcinoma using quantitative dynamic contrast-enhanced magnetic resonance imaging with a point-of-care perfusion phantom: a pilot study. Invest Radiol. 2019;54:16–22.
35. Tang W, Liu W, Li HM, Wang QF, Fu CX, Wang XH, Zhou LP, Peng WJ. Quantitative dynamic contrast-enhanced MR imaging for the preliminary prediction of the response to gemcitabine-based chemotherapy in advanced pancreatic ductal carcinoma. Eur J Radiol. 2019;121:108734.
36. Le Bihan D, Turner R, Douek P, Patronas N. Diffusion MR imaging: clinical applications. AJR Am Journal Roentgenol. 1992;159:591–599.
37. Tofts PS, Berkowitz B, Schnall MD. Quantitative analysis of dynamic Gd-DTPA enhancement in breast tumors using a permeability model. Magn Reson Med. 1995;33:564–568.
38. McConnell H. Relaxation rates by nuclear magnetic resonance. J Chem Phy. 1958;28:430–431.
39. Schneider CA, Rasband WS, Eliceiri KW. NIH Image to ImageJ: 25 years of image analysis. Nat Methods. 2012;9:671–675.
40. Yushkevich PA, Piven J, Hazlett HC, Smith RG, Ho S, Gee JC, Gerig G. User-guided 3D active contour segmentation of anatomical structures: significantly improved efficiency and reliability. Neuroimage. 2006;31:1116–1128.
41. Deoni S. High-resolution T1 mapping of the brain at 3T with driven equilibrium single pulse observation of T1 with high-speed incorporation of RF field inhomogeneities (DESPOT1-HIFI). J Magn Reson Imaging. 2007;26:1106–1111.
42. Paudyal R, Lu Y, Hatzoglou V, Moreira A, Stambuk HE, Oh JH, Cunanan KM, Aramburu Nunez D, Mazaheri Y, Gonen M, Ho A, Fagin JA, Wong RJ, Shaha A, Tuttle RM, Shukla-Dave A. Dynamic contrast-enhanced MRI model selection for predicting tumor aggressiveness in papillary thyroid cancers. NMR Biomed. 2020;33.
43. Klein S, Staring M, Murphy K, Viergever MA, Pluim J. elastix: a toolbox for intensity-based medical image registration. IEEE Trans Med Imaging. 2010;29:196–205.
44. Lee SH, Rimner A, Deasy JO, Hunt MA, Tyagi N. Dual-input tracer kinetic modeling of dynamic contrast-enhanced MRI in thoracic malignancies. J Appl Clin Med Phys. 2019;20:169–188.
45. Paudyal R, Konar AS, Obuchowski NA, Hatzoglou V, Chenevert TL, Malyarenko DI, Swanson SD, LoCastro E, Jambawalikar S, Liu MZ, Schwartz LH, Tuttle RM, Lee N, Shukla-Dave A. Repeatability of quantitative diffusion-weighted imaging metrics in phantoms, head-and-neck and thyroid cancers: preliminary findings. Tomography. 2019;5:15–25.
46. Team RC. R: A Language and Environment for Statistical Computing. R Foundation for Statistical Computing; 2014.
47. Katz MHG, Fleming JB, Bhosale P, Varadhachary G, Lee JE, Wolff R, Wang H, Abbruzzese J, Pisters PWT, Vauthey J-N, Charnsangavej C, Tamm E, Crane CH, Balachandran A. Response of borderline resectable pancreatic cancer to neoadjuvant therapy is not reflected by radiographic indicators. Cancer. 2012;118:5749–5756.
48. Ballehaninna UK, Chamberlain RS. The clinical utility of serum CA 19-9 in the diagnosis, prognosis and management of pancreatic adenocarcinoma: an evidence based appraisal. J Gastrointest Oncol. 2012;3:105–119.
49. Heid I, Steiger K, Trajkovic-Arsic M, Settles M, Eßwein MR, Erkan M, Kleeff J, Jäger C, Friess H, Haller B, Steingötter A, Schmid RM, Schwaiger M, Rummeny EJ, Esposito I, Siveke JT, Braren RF. Co-clinical assessment of tumor cellularity in pancreatic cancer. Clin Cancer Res. 2017;23:1461–1470.
50. Kim H, Mousa M, Schexnailder P, Hergenrother R, Bolding M, Ntsikoussalabongui B, Thomas V, Morgan DE. Portable perfusion phantom for quantitative DCE-MRI of the abdomen. Med Phys. 2017;44:5198–5209.
51. Kim H, Samuel S, Lopez-Casas P, Grizzle W, Hidalgo M, Kovar J, Oelschlager D, Zinn K, Warram J, Buchsbaum D. SPARC-independent delivery of nab-Paclitaxel without depleting tumor stroma in patient-derived pancreatic cancer xenografts. Mol Cancer Ther. 2016;15:680–688.
52. Cao J, Pickup S, Clendenin C, Blouw B, Choi H, Kang D, Rosen M, O'Dwyer PJ, Zhou R. Dynamic contrast-enhanced MRI detects responses to stroma-directed therapy in mouse models of pancreatic ductal adenocarcinoma. Clin Cancer Res. 2019;25:2314–2322.
53. Baxter LT, Jain RK. Transport of fluid and macromolecules in tumors. I. Role of interstitial pressure and convection. Microvasc Res. 1989;37:77–104.
54. Chawla S, Loevner LA, Kim SG, Hwang W-T, Wang S, Verma G, Mohan S, LiVolsi V, Quon H, Poptani H. Dynamic contrast-enhanced MRI-derived intracellular water lifetime (τi): a prognostic marker for patients with head and neck squamous cell carcinomas. AJNR Am J Neuroradiol. 2018;39:138–144.